Magnetic Flux Transport on the Sun

Y.-M. Wang, A. G. Nash, N. R. Sheeley, Jr.

Although most of the magnetic flux observed on the sun originates in the low-latitude sunspot belts, this flux is gradually dispersed over a much wider range of latitudes by supergranular convective motions and meridional circulation. Numerical simulations show how these transport processes interact over the 11-year sunspot cycle to produce a strong "topknot" polar field, whose existence near sunspot minimum is suggested by the observed strength of the interplanetary magnetic field and by the observed areal extent of polar coronal holes. The required rates of diffusion and flow are consistent with the decay rates of active regions and with the rotational properties of the large-scale solar magnetic field.

In 1964, Leighton pointed out that the finite lifetime of supergranular convective cells would give rise to a random walk process that acts to disperse active-region magnetic fields over the solar surface (*1*). Leighton proposed that supergranular "diffusion" alone might account for the migration of magnetic flux across latitudes, which the Babcocks had discovered using their newly developed magnetograph (*2*). During the past decade, however, there has emerged observational evidence for a poleward bulk flow of 10 m/s or more, suggesting that meridional flow also plays an important role in the transport of magnetic flux over the photosphere (*3–5*).

A well-known characteristic of the photospheric magnetic field is that it is clustered into small patches or fragments of high field strength, separated by relatively field-free regions. Thus, on scales less than or on the order of a supergranule diameter (~30,000 km), the magnetic flux is concentrated into sunspots, dense plages within active regions, a "network" bordering the supergranular cells, and smaller, weaker "intranetwork" elements (*6*). On such spatial scales, motions with amplitudes of ~1 km/s are present: these include (for example) the convective motions of granules, diverging flows that sweep magnetic flux to the boundaries of supergranules, outflows from sunspots, and sunspot proper motions. In the present study, we effectively average over this fine structure in order to consider the properties of the sun's large-scale magnetic field, that is, the field as seen at low spatial resolution. Indeed, it is only on scales exceeding the supergranular size that a description of magnetic flux transport in terms of diffusion and global meridional flow becomes meaningful.

The transport of flux across latitudes gives rise to several remarkable features of the sun's large-scale magnetic field.

1) *Spiral patterns.* Streams of magnetic flux spreading poleward from the sunspot belts are deflected eastward by the sun's differential rotation, forming a pattern of slanted stripes, each dominated by a single magnetic polarity (*7*). Such unipolar regions may contain areas of open magnetic field and outward-escaping plasma identified with coronal holes, particularly when their polarity matches that of the adjoining polar region (*8*). Viewed from the equatorial plane, the poleward-moving streams resemble a series of "bow waves" trailing the active regions. Their characteristic backward-C shapes may be seen in Fig. 1, which records the photospheric flux distribution during November 1982, both as observed at the National Solar Observatory (NSO/Kitt Peak) (Fig. 1A) and as simulated by means of the flux-transport model to be described later (Fig. 1B). Viewed alternatively from the direction of the sun's polar axis, the streams form the arms of a spiral pattern converging onto the pole (Fig. 2).

2) *Rigid rotation.* Although the individual magnetic flux elements that make up the spiral patterns rotate differentially at the local photospheric rate, the patterns themselves rotate quasi-rigidly (*7, 9*). This is a kinematic effect, which occurs when a balance is established between the poleward drift of the flux elements and their azimuthal deflection by the rotational shear (*10, 11*). The flux "streamlines" then become stationary in a frame that is rotating at approximately the sun's equatorial rate.

3) *Polar-field reversal.* The continued poleward transport of magnetic flux from one sunspot minimum to the next acts to cancel and reverse the sun's polar field (*2*). According to most solar dynamo models, it is the windup of the poloidal field built up over a sunspot cycle that provides the toroidally oriented flux that erupts during the next cycle (*12*). Sunspot numbers may be correlated with the strength of the polar field at the preceding minimum (*13*).

4) *"Topknot" polar fields.* The polar coronal holes observed around sunspot minimum typically extend down to a latitude of 60°. From the areal size of these open-field regions, it can be shown that the polar field must be highly concentrated, varying with colatitude θ approximately as $\cos^8\theta$ (*14, 15*). A similar result was inferred from the observed annual modulation of the polar field resulting from the sun's axial tilt (*16*). As will be confirmed by our numerical simulations, the maintenance of such a concentrated polar field requires the presence of a poleward bulk flow (*17*). Around the time of sunspot minimum, most of the interplanetary magnetic flux observed at Earth originates from the sun's polar regions (*16, 18*).

Despite their profound influence on the sun's large-scale magnetic field, supergranular diffusion and meridional flow are slow processes whose rates are difficult to measure. Thus, whereas Leighton estimated the diffusion constant to lie between 770 and 1540 km^2/s from the reversal time of the polar field, Mosher (*19*) and DeVore *et al.* (*20*) inferred values of only 200 to 400 km^2/s from the spread of active-region flux (*1*). Doppler measurements of the meridional flow velocity require the removal of a much larger background signal

The authors are in the Space Science Division (Solar Terrestrial Relationships Branch) of the Naval Research Laboratory, Washington, DC 20375.

arising from rotation, granular and supergranular motions, and the 5-min oscillation; and there may be spurious contributions to the spectral line shifts caused by temperature inhomogeneities, magnetic fields, and scattered light (*3*). The use of magnetic tracers to detect global velocity fields requires that the effects of flow and diffusion be properly separated (*4, 5*).

In this study, we obtain further constraints on the flux-transport rates by comparing our numerical simulations with low-resolution, synoptic magnetic data from the Mount Wilson Observatory (MWO) and the Wilcox Solar Observatory (WSO). We find that the diffusion constant is 600 ± 200 km^2/s, whereas the poleward flow has an average amplitude of 10 ± 3 m/s. These transport rates allow us to account quantitatively for the following properties of the sun's large-scale field: (i) the dispersal and decay of magnetic flux from individual active regions; (ii) the evolution of the sun's axisymmetric dipole field over sunspot cycle 21 (1976 to 1986) and the latitudinal distribution of the polar field at the end of the cycle; and (iii) the rotation rates of the photospheric and coronal magnetic fields.

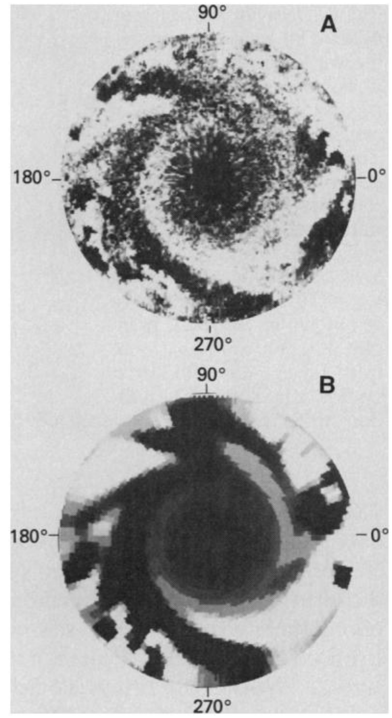

Fig. 2. Northern Hemisphere flux distribution during November 1982, pole-centered view. Latitude scales linearly with radial distance from the map perimeter, which coincides with the equator. The logarithmic gray scale is similar to that used in Fig. 1. (**A**) Observed intensities. (**B**) Simulated intensities (same parameters as in Fig. 1B).

The Flux-Transport Model

We calculate the evolution of the radial component of the photospheric field, $B(\theta,\phi,t)$, by numerically integrating the flux-transport equation (*1, 17, 21*):

$$\frac{\partial B}{\partial t} = -\,\omega(\theta)\,\frac{\partial B}{\partial \phi} - \frac{1}{R_\odot \sin\theta}\,\frac{\partial}{\partial \theta}[\nu(\theta) B \sin\theta] + \frac{\kappa}{R_\odot^{2}}\left[\frac{1}{\sin\theta}\,\frac{\partial}{\partial\theta}\left(\sin\theta\,\frac{\partial B}{\partial\theta}\right) + \frac{1}{\sin^{2}\theta}\,\frac{\partial^{2}B}{\partial\phi^{2}}\right] + S(\theta,\phi,t) \qquad (1)$$

Here θ is colatitude, ϕ is longitude measured westward (in the direction of the solar rotation), $R_\odot$ is the sun's radius, $\omega(\theta)$ is the angular rotation rate of the photospheric plasma, $\nu(\theta)$ is the meridional flow velocity, κ is the effective diffusion constant associated with the nonstationary supergranular convection, and $S(\theta,\phi,t)$ is a source term that describes the emergence of new bipolar magnetic regions.

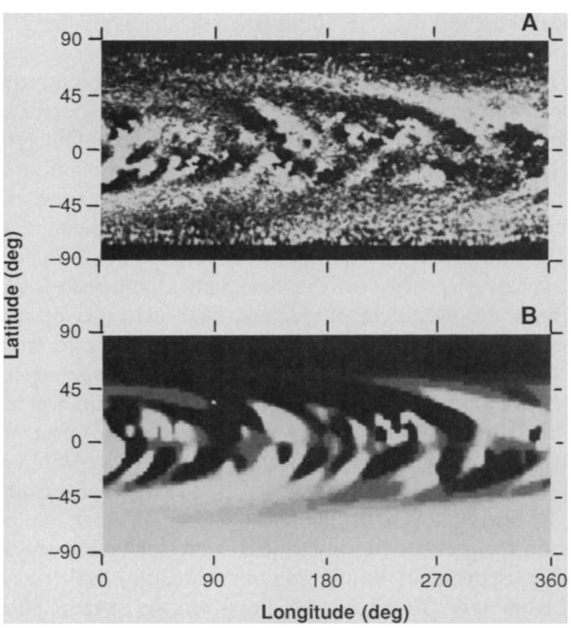

Fig. 1. Photospheric flux distribution during November 1982. Radial-field intensities are represented by a logarithmic gray scale, with contours ranging from $B < -50$ G (black) to $B > 50$ G (white). (**A**) High-resolution synoptic map constructed from daily NSO/Kitt Peak magnetograms taken during Carrington rotation 1728. The horizontal strips at the top and bottom of the map indicate the absence of reliable flux measurements within 12° of the poles. (**B**) Instantaneous map obtained by simulating the evolution of the photospheric field with transport parameters $\kappa = 600$ km^2/s, $\nu_m = 10$ m/s, $p = 1$, and $q = 0.01$.

We assume that the synodic rotation rate of individual flux elements is described by the empirical formula of Snodgrass (*22*),

$$\omega(\theta) = 13.38 - 2.30\cos^{2}\theta - 1.62\cos^{4}\theta \ \text{deg/day} \qquad (2)$$

The meridional flow velocity is taken to be antisymmetric across the equator and of the form

$$\nu(\theta) = -\,\nu_{\mathrm{m}}\left(\frac{\sin\theta}{\sin\theta_{\mathrm{m}}}\right)^{p}\left(\frac{\cos\theta}{\cos\theta_{\mathrm{m}}}\right)^{q} \ (\theta \le \pi/2) \qquad (3)$$

where ν_{m} denotes the peak flow speed attained at colatitude θ_{m}, and p and q are parameters to be specified later. The possibility of a nonsteady meridional flow on the sun is not considered here.

Assuming an initial field configuration, we perform the computations on a rectangular grid representing the entire photosphere and consisting of 128 cells equally spaced in longitude and 64 cells equally spaced in latitude. Our aim is to determine the values of the parameters κ, ν_{m}, p, and q by simulating observed properties of the sun's large-scale magnetic field.

The Decay of Active-Region Flux

A direct way of estimating the diffusion constant κ is to model the spread and decay of magnetic flux from observed active regions. For this purpose, we require strong, isolated, reasonably low-latitude regions that evolved for a few rotations without substantial new eruptions of flux. These rather stringent conditions limit the choice to a small number of bipolar magnetic regions appearing near sunspot minimum. For detailed modeling, we selected four regions having the following National Oceanic and Atmospheric Administration–U.S. Air Force Sunspot Group designations, dates of first central-meridian passage, and approximate latitudes: 4656 (23 May 1985; 7°N), 4723 (14 April 1986; 12°S), 4750 (23 October 1986;

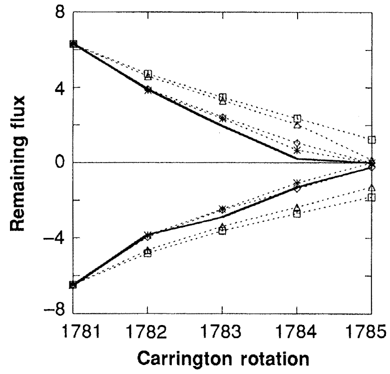

Fig. 3. Decay of active region 4750. The total flux remaining within contours of ±3 G is shown as a function of Carrington rotation. The unit of magnetic flux is 10^{21} G-cm^2. The observed decay curves, derived from MWO Carrington maps, are indicated by the thick lines. The simulated decay curves are keyed as follows: asterisks ($\kappa = 600$ km^2/s, $v_m = 10$ m/s); diamonds ($\kappa = 600$ km^2/s, no flow); triangles ($\kappa = 300$ km^2/s, $v_m = 10$ m/s); boxes ($\kappa = 300$ km^2/s, no flow). In all four cases, the flow profile parameters were assigned the values $p = 1$, $q = 0.01$.

23°N), and 4789 (13 April 1987; 6°S). The observations consisted of Carrington (27.275-day) synoptic maps of the line-of-sight photospheric field, compiled at MWO and WSO from central meridian–weighted daily magnetograms. The resolution of these photospheric maps was 91 pixels in longitude by 34 pixels in sine latitude (MWO) and 72 pixels in longitude by 30 pixels in sine latitude (WSO). The large-scale field was assumed to be primarily radial at the photosphere, as inferred observationally by Howard and LaBonte (*4*).

After dividing the photospheric field strengths by sinθ to convert the line-of-sight values into radial ones, we interpolated the observed synoptic maps onto the 128×64 numerical grid and used the map containing the first central-meridian passage of the active region under study as the initial field configuration in the simulation. This photospheric map was evolved according to Eq. 1, with the source term S set equal to zero and with trial values of the parameters κ and v_m adopted. The numerically evolved active region was then compared at 27.275-day intervals with the corresponding region on the observed Carrington maps.

As an example, we consider the evolution of active region 4750 during Carrington rotations 1781 to 1785. Figure 3 shows how the total magnetic flux within contours of +3 G (upper curves) and −3 G (lower curves) decayed from one rotation to the next. The residual fluxes, in units of 10^{21} G-cm^2, have been calculated for four illustrative choices of the transport parameters (κ, v_m). (The simulated decay rates were found to be insensitive to the parameters describing the flow profile, which were assigned the values $p = 1$ and $q = 0.01$ in accordance with the discussion of the next section.) For comparison, Fig. 3 also shows the observed residual fluxes, as derived from the corresponding MWO Carrington maps. It is apparent that the observed decay rate is better matched with a diffusion constant of 600 km^2/s than with one of 300 km^2/s. In addition, we found that the inclusion of a 10 m/s poleward flow, while only slightly accelerating the decay rates shown in Fig. 3, greatly improved the agreement between the spatial patterns of the simulated and observed active regions over time spans greater than a month (*23*).

For the remaining three active regions that we studied, we obtained best-fit values of the diffusion rate ranging from 400 to 750 km^2/s and poleward flow speeds ranging from 5 to 15 m/s. Averaging all of these results, we conclude that $\kappa = 600 \pm 200$ km^2/s and $v_m = 10 \pm 5$ m/s (where the error estimates are 3 SE). In general, values of κ much below 600 km^2/s cause the remnant flux to decay too slowly, whereas larger diffusion rates dissipate the flux too rapidly. The inclusion of meridional flow improves the spatial correlation between the simulated and observed flux distributions, because not only do the polarity centroids of an observed active region spread apart under the action of supergranular diffusion and differential rotation but both poles also drift slowly to higher latitudes.

By applying a similar model to NSO daily magnetograms during 1974 to 1977 and maximizing correlation coefficients, DeVore *et al.* derived values of κ that were mostly in the range 200 to 400 km^2/s (*20*). The probable reason for the discrepancy with the results of the present study is that the high-resolution NSO data show much smaller scale structure than can be reproduced with the use of Eq. 1. This may have made it necessary for DeVore *et al.* to lower their diffusion rates artificially in order to account for the extra flux appearing on the NSO magnetograms. Our use of observations whose spatial resolution is more compatible with that of the simulations allows the observed and simulated remnant fluxes to be compared consistently and also improves the agreement between the spatial patterns of the dispersing active regions.

Meridional Flow and the Polar Field

There is now considerable evidence that the sun has a strong, highly concentrated polar field around sunspot minimum. By analyzing WSO observations of the line-of-sight field above 55° latitude, Svalgaard *et al.* concluded that the flux distribution had the form ± 11.5 G $\cos^8\theta$ during the period 1976 to 1977, consistent with the average polar-cap field strength of 5 G that Giovanelli later derived from NSO magnetograms taken in January 1976 (*16, 24*). More recent WSO measurements that we use below suggest that the polar field was even stronger and more peaked in 1986 than during 1976 to 1977. A concentrated polar field is also consistent with the areal sizes of the polar coronal holes observed around sunspot minimum and with the occurrence of high-latitude enhancements in the He I 10830 Å network, which mark the location of strong polar-cap fields that have become reconnected to new cycle active regions (*14, 15*). Finally, a strong polar field is required to account for the observed strength of the interplanetary magnetic field around sunspot minimum (*16, 18*).

We now show that the buildup of a strong, concentrated polar field near sunspot minimum requires flux to be transported both by supergranular diffusion and by a poleward bulk flow. Our procedure is to evolve the photospheric field according to Eq. 1 from August 1976 to April 1986, depositing magnetic doublet sources onto the computational grid at their observed locations and times of eruption. The initial field configuration was taken to be of the form $B = \pm 11.5$ G $\cos^8\theta$ (positive in the Northern Hemisphere), in agreement with the WSO measurements. The strengths of the 2800 doublet sources used in the simulations were estimated empirically from NSO daily magnetograms (*21*). The computations were repeated with different values of the transport parameters κ, v_m, p, and q, and the results compared with WSO synoptic observations of the photospheric field during sunspot cycle 21. The WSO measurements were multiplied by a factor of 1.8 to correct for the saturation of the Fe I 5250-Å line profile (*15*).

As one measure of the polar-field evolution, we calculated the vertical (axisymmetric) dipole strength of the photospheric field as a function of time. This quantity shows less short-term fluctuation than the mean polar-cap field strength (*25*). In Fig. 4A, the observed monthly values of the vertical-dipole strength are shown together with simulated curves based on the following choices of the transport parameters: $\kappa = 600$ km^2/s, no flow; $\kappa = 600$ km^2/s, $v_m = 10$ m/s; and $\kappa = 300$ km^2/s, $v_m = 10$ m/s (in every case, we have taken $p = 1$, $q = 0.01$). As another polar-field diagnostic, we compare the observed and simulated latitude distributions of the photospheric field late in sunspot cycle 21 (Fig. 4B). Here the fields have been averaged over longitude and over the time interval September 1985 to March 1986.

The best fits to both the average long-term evolution of the dipole field and the final latitudinal distribution of the axisymmetric field are provided by a diffusion rate of 600 km²/s combined with a poleward flow of amplitude 10 m/s. In the case where diffusion alone is present, the dipole reverses its polarity at the beginning of 1979, about a year earlier than observed; also, the final polar-field distribution in 1986 is much flatter than observed. When a 10 m/s poleward flow is included but the diffusion constant is only 300 km²/s, the dipole reverses 2 years later than observed and the final polar field is too weak.

In order to explain these results, we first note that bipolar magnetic regions on the sun normally emerge with their westward pole (which "leads" in the direction of rotation) located a few degrees equatorward of their trailing pole and with their dipole moments oriented opposite to the sun's polar field at the preceding sunspot minimum (*2, 26*). This configuration is consistent with the idea that the bipoles represent loops from a submerged, azimuthally oriented field, which is antisymmetric about the equator and formed by winding up the poloidal field built up during the preceding sunspot cycle (*12*). During sunspot cycle 21, the trailing flux had negative polarity in the Northern Hemisphere and positive polarity in the Southern Hemisphere. The preferential transport of this higher latitude, trailing flux to the poles over the sunspot cycle reversed the overall polarity of the sun's magnetic field, which was initially positive in the north.

If a strong meridional flow but little diffusion were present on the sun, the leading and trailing fluxes in each hemisphere would be carried poleward in nearly equal amounts and the two polarities would largely cancel each other (*27*). This explains why the simulation with $\nu_m = 10$ m/s and $\kappa = 300$ km²/s only barely managed to reverse the dipole moment and produced a relatively weak polar field in 1986. By contrast, if a strong diffusion but no poleward flow were present, the lower latitude, leading fluxes in the two hemispheres would spread freely across the equator and annihilate each another. This would leave a large surplus of trailing-polarity flux in each hemisphere, which would rapidly neutralize the original polar field and build up a strong dipole moment of the opposite polarity. As demonstrated by the simulation with $\kappa = 600$ km²/s and no flow, however, the new latitudinal distribution would be relatively flat because steep poleward gradients in the field cannot be maintained without flow. Thus, the combination of large diffusion and poleward flow rates represents a compromise that leads to both a strong dipole moment and a sharply peaked polar field.

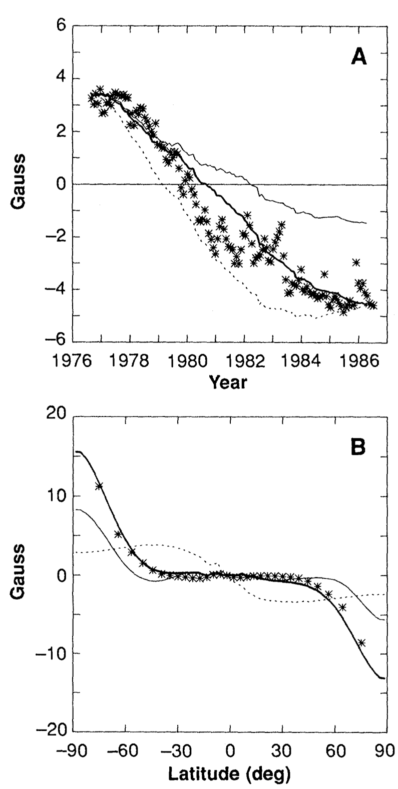

Fig. 4. Evolution of the polar field during sunspot cycle 21. (**A**) Time evolution of the vertical-dipole component of the photospheric field (the ordinate gives the axial strengths in gauss). Asterisks designate observed monthly strengths, determined from the corresponding WSO Carrington maps and including the line-saturation correction factor of 1.8. Simulated values are indicated by the thick line ($\kappa = 600$ km²/s, $\nu_m = 10$ m/s); thin line ($\kappa = 300$ km²/s, $\nu_m = 10$ m/s); and dotted line ($\kappa = 600$ km²/s, no flow). In all three cases, the flow profile parameters were assigned the values $p = 1$, $q = 0.01$. (**B**) Latitudinal distribution of the (longitudinally averaged) photospheric field near the end of sunspot cycle 21. The radial-field strengths have been averaged over the time interval September 1985 to March 1986. Asterisks indicate the WSO measurements, and the three curves represent the simulated field distributions for the same parameters as in (A). [The observed quantities shown in (A) and (B) are relatively insensitive to the annual modulation arising from the sun's 7° polar tilt, which has not been corrected for when converting the line-of-sight field strengths into radial ones.]

From our modeling of the polar fields measured at WSO, we deduce that $\kappa = 600$ km²/s and $\nu_m = 10$ m/s. Allowing for systematic errors in the doublet-strength determinations, we estimate the uncertainties in these quantities to be ± 200 km²/s and ± 3 m/s, respectively. Although we did not attempt a detailed optimization of the parameters p and q, we found that the observed polar-field distribution in 1986 was best matched with a flow profile that peaks close to the equator and declines toward higher latitudes: this is illustrated by our choice $p = 1$, $q = 0.01$. Flow profiles that were significantly flatter or that peaked at mid-latitudes were found to give too strong a polar field.

The high-latitude field strengths measured at MWO after 1982 were less than two-thirds of the WSO strengths for the same period and would imply substantially lower transport rates (on the order of $\kappa = 300$ km²/s and $\nu_m = 7$ m/s). Although we cannot explain the discrepancy between the two data sets, we note that the WSO measurements show an evolutionary trend consistent with the variation of the interplanetary magnetic field but the MWO measurements do not. In particular, the MWO polar fields were somewhat weaker near the 1986 sunspot minimum than near the 1976 one, whereas the WSO polar fields and the interplanetary magnetic field were both 30 to 40% stronger (*18, 28*). Because the sun's polar fields provide most of the interplanetary magnetic flux around sunspot minimum, this suggests that the MWO measurements were in error after 1982 or during 1976 to 1978.

In an earlier study, DeVore and Sheeley found that the evolution of the WSO and MWO polar fields during 1976 to 1984 could be simulated with transport rates of $\kappa = 300$ km²/s and $v_m = 10$ m/s (*27*). Our results differ from theirs because we have corrected the observed fields for line saturation, which increases the field strengths and implies correspondingly larger values of κ or smaller values of ν_m.

Rotation of the Photospheric and Coronal Fields

The poleward-drifting streams of active-region flux merge to form a series of broad unipolar channels, which are sheared back by the sun's differential rotation. The resulting backward-C structures may be seen in the equatorially centered maps of Fig. 1, where we display the photospheric flux distribution during Carrington rotation 1728 (November 1982), both as observed at NSO and as simulated on the basis of the transport rates derived in the previous section. Viewed from above the North Pole (Fig. 2), the curved unipolar bands form a spiral pattern converging onto the negative-polarity polar cap. In these figures, the simulated maps do not show the fine-scale magnetic structure of the observed maps, but the large-scale patterns are very similar.

We now demonstrate that the observed flux patterns rotate quasi-rigidly at rates consistent with our choice of the transport parameters. By cross-correlating monthly pairs of WSO Carrington maps in longitude and averaging the results over the 2-year intervals 1978 to 1979 and 1984 to 1985, we obtained the rotation profiles of the observed photospheric field. These are compared in Fig. 5 with the corresponding profiles found by simulating the evolution of the photospheric field, taking $\kappa = 600$ km^2/s, $v_m = 10$ m/s, $p = 1$, and $q = 0.01$. Figure 5 also shows the rotation curve given by Eq. 2, which Snodgrass derived by cross-correlating magnetograms taken only a few days apart rather than at monthly intervals (*22*).

From Fig. 5, it is apparent that both the observed and simulated rotation profiles (based on monthly cross-correlations) are more rigid than the Snodgrass curve, pulling off from it increasingly at higher latitudes. The difference reflects the fact that the Snodgrass formula describes the motion of individual flux elements that follow the motion of the photospheric plasma; these relatively intense, small-scale features dominate the field observed with high resolution but have lifetimes of only a few days. In contrast, the monthly cross-correlations pick out weaker but longer lived patterns, whose structure and rotation are determined by latitudinal flux-transport processes. These large-scale patterns may be identified with the crescent-shaped unipolar regions described above.

The physical explanation for the rigid rotation of the large-scale field is that, in the absence of new flux eruptions, the shearing of the flux distribution by differential rotation is gradually counteracted by the steady drift of flux across latitudes (*10, 11*). Thus the flux "streamlines" or lines of constant phase become approximately stationary in the equatorial frame for streamlines originating near the equator. (In fact, the asymptotic configuration is bimodal. As flux accumulates at the poles, a net equatorward diffusion is set up there, and the polar zone rotates quasi-rigidly at approximately the polar rate.)

The time scale τ_r for rigid rotation to be established may be estimated by dimensional analysis of Eq. 1, taking $S = 0$ (*11*). For this purpose, it is convenient to define global times scales for windup, $\tau_w \equiv 2\pi/[\omega(\pi/2) - \omega(0)]$, for meridional flow, $\tau_f \equiv R_\odot/v_m$, and for diffusion, $\tau_d \equiv R_\odot^2/\kappa$. For simplicity, we suppose that the flux distribution is initially proportional to $\cos(m\phi)$ and thus has $2m$ longitudinal polarity sectors. As windup proceeds, azimuthally oriented stripes are formed at a rate m/τ_w and the latitudinal gradients in the field steepen correspondingly. After a time $t \sim \tau_r$, the latitudinal transport rates balance the shearing rate, and there are $\sim m\tau_r/\tau_w$ stripes of each polarity. The meridional field gradient is then given by $\partial B/\partial\theta \sim m\tau_r B/\tau_w$, while the azimuthal gradient remains $\partial B/\partial\phi \sim mB$. Thus, if we neglect diffusion and equate the shearing and flow terms in Eq. 1, we find that $\tau_r \sim \tau_f$, where τ_f = 2.2 years for a flow speed $v_m = 10$ m/s. In this idealized case where only a poleward flow is present, the local pitch of the rigidly rotating stripes is given by $d\phi/d\theta = [\omega(\theta) - \omega(\pi/2)]R_\odot/v(\theta)$.

Alternatively, neglecting flow but including diffusion, one finds by balancing the shearing and latitudinal diffusion terms that rigid rotation is attained on a time scale $\tau_r \sim (\tau_w\tau_d/m\pi)^{1/2}$. [Here we have inserted an extra factor of $\pi^{-1/2}$ obtained from a more rigorous time-asymptotic analysis of Eq. 1 (*11*).] Evaluating this expression with $\kappa = 600$ km^2/s, $m \sim 10$ (as typically observed for the photospheric field), and a shearing profile given by Eq. 2, we obtain $\tau_r \sim$ 5 months, which is somewhat longer than the windup time $\tau_w \sim 3$ months but much shorter than the global diffusion time $\tau_d \sim 24$ years. As shown by DeVore (*11*), τ_r is also the time scale for the decay of the nonaxisymmetric field by shearing and diffusive annihilation.

The effect of source eruptions is to impede the buildup of the latitudinal phase gradients required for rigid rotation (*10*). Thus, if the flux in a given region is constantly being rejuvenated on a time scale much shorter than τ_r, the local "streamlines" will not be able to attain the azimuthal pitch that brings them into equilibrium with the rotational shear. This explains why the rotation rate of the large-scale photospheric field closely follows the differential Snodgrass rate in the sunspot belts. We can likewise understand why the profiles become more rigid during the declining phase of the sunspot cycle and pull off the Snodgrass curve at progressively lower latitudes (compare Fig. 5A and 5B).

Next, we demonstrate that our transport model is also consistent with the rotational properties of the coronal magnetic field. In general, coronal structures are observed to rotate more rigidly than the underlying photosphere (*29*). This behavior is a consequence of the dominance of low-order multipoles with increasing height, a property of the coronal field that is consistent with its largely current-free nature (*30*). Such low-order multipoles represent globally averaged properties of the photospheric flux distribution and rotate at rates characteristic of the low latitudes where the bulk of the sun's large-scale, nonaxisymmetric flux is concentrated. These latitudes may be somewhat displaced from the sunspot belts, because new, undispersed active-region fields are dominated by high-order multipoles. Toward sunspot minimum, the nonaxisymmetric flux influencing the coronal rotation will be localized around the equator; earlier in the sunspot cycle, it will be located just poleward of the sunspot belts, where the broad unipolar stripes begin to form. Because the photospheric rotation is relatively rigid at these latitudes, the coronal field shows a correspondingly limited spread of rotation rates. At higher latitudes, increased rotational shearing rapidly transfers power to higher order multipoles, which are "filtered" out of the corona.

To obtain the magnetic field in the corona, we use the current-free approximation to extrapolate the known photospheric flux distribution out to a spherical "source surface" $r = R_s$, where the nonradial components of the field vanish (*31*). Choosing $R_s = 2.5\ R_\odot$, we perform monthly cross-correlations to obain the rotation rates of the source-surface field. Figure 6 shows the resulting average rotation profiles during 1978 to 1979 and 1984 to 1985, as derived from WSO Carrington maps of the photospheric field and from our photospheric simulations with $\kappa = 600$ km^2/s, $v_m = 10$ m/s, $p = 1$, and $q = 0.01$. The transport parameters were chosen so as to optimize the agreement between the "observed" and simulated coronal rotation profiles during sunspot cycle 21, and they agree

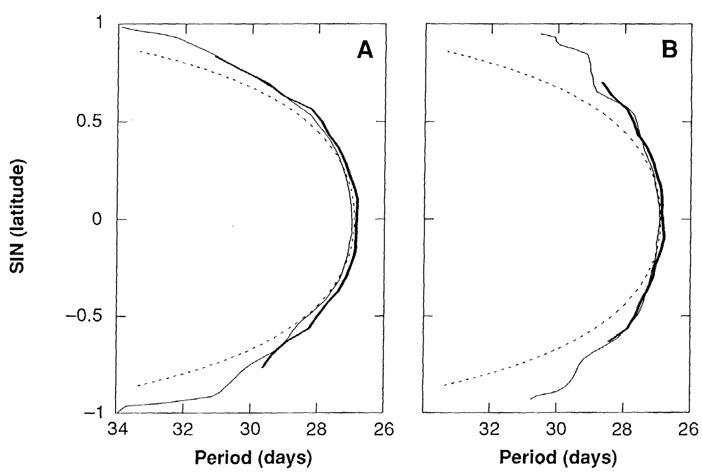

Fig. 5. Average rotation profiles of the photospheric field, (**A**) during 1978 to 1979 and (**B**) during 1984 to 1985. Thick lines are observed profiles, obtained by cross-correlating consecutive pairs of WSO Carrington maps. Thin lines are simulated profiles, obtained by solving the flux-transport equation with $\kappa = 600$ km^2/s, $v_m = 10$ m/s, $p = 1$, and $q = 0.01$. The dotted curve is the Snodgrass formula describing the rotation of individual flux elements (*22*).

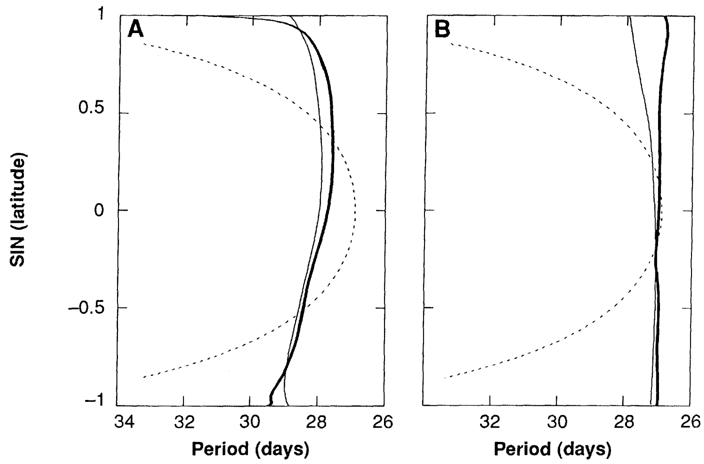

Fig. 6. Average rotation profiles of the coronal field at $r = 2.5\ R_\odot$, (**A**) during 1978 to 1979 and (**B**) during 1984 to 1985. Thick lines are profiles obtained by extrapolating the WSO photospheric observations to a source surface located at $2.5\ R_\odot$ and cross-correlating the resulting monthly maps. Thin lines are profiles obtained by applying a similar procedure to the simulated photospheric field, for transport parameters $\kappa = 600$ km^2/s, $v_m = 10$ m/s, $p = 1$, and $q = 0.01$. The dotted curve is the photospheric rotation rate of Snodgrass (*22*).

with the values derived earlier in this article.

It is apparent from Fig. 6 that the source-surface field rotates far more rigidly than the photosphere. The differences between the rotation profiles for 1978 to 1979 and 1984 to 1985 are related to changes in the location and intensity of sunspot activity. During the earlier interval, sunspot eruptions occurring at an average latitude of ~20° continually inject nonaxisymmetric flux, which drifts poleward, spreads in longitude, and becomes increasingly sheared. The centroid of the large-scale, nonaxisymmetric flux is then located just poleward of the sunspot belts. As a result, the coronal rotation profiles are shifted toward longer periods and display a relatively large amount of curvature and asymmetry, reflecting the photospheric differential rotation at those latitudes. With declining sunspot activity, however, the combined effect of windup and diffusion causes the mid-latitude flux to decay on the time scale τ_r and the locus of the nonaxisymmetric flux migrates toward the equator. The rotation of the coronal field becomes correspondingly faster and more rigid and approaches the 27-day equatorial period at all latitudes.

We can now understand why coronal holes, representing the footpoint areas of "open" field lines, are also observed to rotate more rigidly than the photospheric field (*32*). Because the tenuous corona cannot support large volume currents, these footpoints will tend to corotate with the source-surface regions to which they are magnetically connected: otherwise, if the holes were to deform at the local photospheric rate, the coronal magnetic field would become increasingly sheared and the curl-free condition would be violated (*14*). Thus, the source-surface field lines must continually change their footpoint connections ("reconnect") to untie their motion from that of the photosphere. In effect, a coronal hole moves as a kind of "reconnection wave" rather than as a material region rooted in the photosphere. The required reconnections take place high in the corona and involve interchanges between open field lines at the hole boundary and neighboring loops that close just below the source surface. In such exchanges, the lower segment of an open field line closes down by reconnecting to the far leg of an adjacent closed loop, while the upper segment of the open field line reconnects to the near leg of the severed loop, which thereby opens out to become part of the hole. The resulting deformation of the hole boundary will be such as to oppose the shearing effect of the photospheric differential rotation.

In short, we may regard a coronal hole as a pattern of open field footpoints that "shadows" the source-surface field, whose quasi-rigid rotation is in turn determined by the global distribution of photospheric flux. It is therefore not surprising that the tendency for the source-surface field to rotate faster as the sunspot cycle progresses is also reflected in the rotation of coronal holes, whose periods typically decrease from ~28.5 days during the rising and maximum phases of the cycle, to ~27 days toward sunspot minimum. Large holes formed during the declining phase of the cycle give rise to high-speed wind streams and associated geomagnetic activity characterized by a 27-day recurrence pattern (*33*).

Concluding Remarks

By comparing observed and simulated properties of the sun's large-scale magnetic field, we have found that the supergranular diffusion rate is 600 ± 200 km^2/s and that the average amplitude of the poleward surface flow is 10 ± 3 m/s. With these transport rates, we were able to simulate the long-term evolution of the polar fields, the formation of spiral patterns, and the rotation of the large-scale photospheric and coronal fields, without introducing ad hoc assumptions about subsurface phenomena that are as yet poorly understood.

Although the flux-transport model provides useful insights into the nature of the sun's large-scale magnetic field, it breaks down on scales comparable to a supergranule size, where interactions between individual "fragments" of magnetic flux take place in localized flow fields. High-resolution observations and modern image-processing techniques are now making it possible to study these complex small-scale flows in detail. A "kinetic theory" that relates the "molecular" interactions on the supergranular scale to the large-scale transport rates needs to be developed.

Ultimately, we would like to understand the relation between the flux-transport processes on the photosphere and the hidden internal mechanisms that drive the solar cycle. The nature of the sun's internal magnetic field and the processes that cause sunspot-belt flux to erupt as observed remain enigmatic. Continued long-term synoptic studies of solar activity and future helioseismological observations should eventually provide some answers to these questions.

REFERENCES AND NOTES

1. R. B. Leighton, *Astrophys. J.* **140**, 1547 (1964).
2. H. W. Babcock and H. D. Babcock, *ibid.* **121**, 349 (1955).
3. T. L. Duvall, Jr., *Sol. Phys.* **63**, 3 (1979); B. J. LaBonte and R. Howard, *ibid.* **80**, 361 (1982); R. S. Bogart, *ibid.* **110**, 23 (1987); R. K. Ulrich *et al.*, *ibid.* **117**, 291 (1988).
4. R. Howard and B. J. LaBonte, *ibid.* **74**, 131 (1981).
5. K. Topka, R. Moore, B. J. LaBonte, R. Howard, *ibid.* **79**, 231 (1982).
6. H. Zirin, *Astrophysics of the Sun* (Cambridge Univ. Press, Cambridge, 1988), chap. 6; C. Zwaan, *Annu. Rev. Astron. Astrophys.* **25**, 83 (1987).
7. V. Bumba and R. Howard, *Astrophys. J.* **141**, 1502 (1965).
8. P. S. McIntosh, A. S. Krieger, J. T. Nolte, G. Vaiana, *Sol. Phys.* **49**, 57 (1976); J. D. Bohlin and N. R. Sheeley, Jr., *ibid.* **56**, 125 (1978).
9. R. Howard, *Annu. Rev. Astron. Astrophys.* **22**, 131 (1984); E. H. Schröter, *Sol. Phys.* **100**, 141 (1985).
10. N. R. Sheeley, Jr., A. G. Nash, Y.-M. Wang, *Astrophys. J.* **319**, 481 (1987).
11. C. R. DeVore, *Sol. Phys.* **112**, 17 (1987).
12. H. W. Babcock, *Astrophys. J.* **133**, 572 (1961); R. B. Leighton, *ibid.* **156**, 1 (1969); E. N. Parker, *Cosmical Magnetic Fields* (Clarendon, Oxford, 1979), chap. 21.
13. K. H. Schatten and S. Sofia, *Geophys. Res. Lett.* **14**, 632 (1987).
14. A. G. Nash, N. R. Sheeley, Jr., Y.-M. Wang, *Sol. Phys.* **117**, 359 (1988).
15. N. R. Sheeley, Jr., Y.-M. Wang, J. W. Harvey, *ibid.* **119**, 323 (1989).
16. L. Svalgaard, T. L. Duvall, Jr., P. H. Scherrer, *ibid.* **58**, 225 (1978).
17. C. R. DeVore, N. R. Sheeley, Jr., J. P. Boris, *ibid.* **92**, 1 (1984).
18. Y.-M. Wang and N. R. Sheeley, Jr., *J. Geophys. Res.* **93**, 11227 (1988).
19. J. M. Mosher, thesis, California Institute of Technology (1977).
20. C. R. DeVore *et al.*, *Sol. Phys.* **102**, 41 (1985).
21. N. R. Sheeley, Jr., C. R. DeVore, J. P. Boris, *ibid.* **98**, 219 (1985).

22. H. B. Snodgrass, *Astrophys. J.* **270**, 288 (1983).
23. W. H. Marquette and S. F. Martin [*Sol. Phys.* **117**, 227 (1988)] have presented a detailed observational study of active region 4750, in which they concluded that a substantial fraction of the trailing polarity flux migrated equatorward and south of the leading polarity flux, in contradiction to the behavior expected from the diffusion model of Leighton (*1*). We believe that the most likely explanation for their observation is that new flux erupted on the equatorward side of the active region during its first passage or while it was behind the solar limb during early November 1986. In order to allow for this possibility, we initialized our simulation of this active region at Carrington rotation 1782 (rather than 1781) and again obtained a best-fit diffusion constant of order 600 km^2/s over the succeeding three rotations.
24. R. G. Giovanelli, *ibid.* 77, 27 (1982).
25. The magnetograph data show that the polar-cap fields underwent large fluctuations just after sunspot maximum. Subsequent work suggests that these oscillations were caused by an acceleration of the meridional flow rate during 1980 to 1982 (Y.-M. Wang, A. G. Nash, N. R. Sheeley, Jr., *Astrophys. J.*, in press). The present model remains a valid description of the long-term evolution of the polar fields.
26. G. E. Hale, F. Ellerman, S. B. Nicholson, A. H. Joy, *ibid.* **49**, 153 (1919).
27. C. R. DeVore and N. R. Sheeley, Jr., *Sol. Phys.* **108**, 47 (1987).
28. J. A. Slavin, G. Jungman, E. J. Smith, *Geophys. Res. Lett.* **13**, 513 (1986).
29. E. Antonucci and L. Svalgaard, *Sol. Phys.* **34**, 3 (1974); G. D. Parker, R. T. Hansen, S. F. Hansen, *ibid.* **80**, 185 (1982); R. Fisher and D. G. Sime, *Astrophys. J.* **287**, 959 (1984); J. T. Hoeksema and P. H. Scherrer, *ibid.* **318**, 428 (1987).
30. Y.-M. Wang, N. R. Sheeley, Jr., A. G. Nash, L. R. Shampine, *Astrophys. J.* **327**, 427 (1988).
31. K. H. Schatten, J. M. Wilcox, N. F. Ness, *Sol. Phys.* **6**, 442 (1969); M. D. Altschuler and G. Newkirk, *ibid.* **9**, 131 (1969); J. T. Hoeksema, thesis, Stanford University (1984).
32. A. S. Timothy, A. S. Krieger, G. S. Vaiana, *Sol. Phys.* **42**, 135 (1975); W. J. Wagner, *Astrophys. J.* **198**, L141 (1975); J. D. Bohlin, *Sol. Phys.* **51**, 377 (1977).
33. J. B. Zirker, Ed., *Coronal Holes and High Speed Wind Streams* (Colorado Associated Universities Press, Boulder, 1977); W. C. Feldman, J. R. Asbridge, S. J. Bame, J. T. Gosling, *J. Geophys. Res.* **83**, 2177 (1978); N. R. Sheeley, Jr., and J. W. Harvey, *Sol. Phys.* **70**, 237 (1981).
34. We are indebted to C. R. DeVore for his role in developing the flux-transport code and for his continuing advice. We also thank J. E. Boyden and R. K. Ulrich (MWO/University of California, Los Angeles), J. W. Harvey (NSO/Kitt Peak), and P. H. Scherrer and J. T. Hoeksema (WSO/Stanford) for providing the magnetograph data used here. This research was supported by the Solar Physics Branch of the National Aeronautics and Space Administration Space Physics Division (DPR W-14429) and by the Office of Naval Research.

Morphogenesis of the Polarized Epithelial Cell Phenotype

ENRIQUE RODRIGUEZ-BOULAN AND W. JAMES NELSON

Polarized epithelial cells play fundamental roles in the ontogeny and function of a variety of tissues and organs in mammals. The morphogenesis of a sheet of polarized epithelial cells (the trophectoderm) is the first overt sign of cellular differentiation in early embryonic development. In the adult, polarized epithelial cells line all body cavities and occur in tissues that carry out specialized vectorial transport functions of absorption and secretion. The generation of this phenotype is a multistage process requiring extracellular cues and the reorganization of proteins in the cytoplasm and on the plasma membrane; once established, the phenotype is maintained by the segregation and retention of specific proteins and lipids in distinct apical and basal-lateral plasma membrane domains.

THE STRUCTURAL AND FUNCTIONAL POLARITY OF EPITHELIAL cells is important in the vectorial function of a variety of mammalian organs and tissues. Studies have been carried out on polarized epithelial cells in vivo (in liver, intestine, kidney, and preimplantation mouse embryos) and in vitro with cultures of kidney [Madin-Darby canine kidney (MDCK), LLC-PK1, and others] and intestinal (HT-29, T-84, and Caco2) cells (*1*). These studies have shown that the polarized epithelial cell phenotype is characterized by (Fig. 1) (i) the distribution of plasma membrane proteins and lipids to three distinct surface domains, apical, lateral, and basal; (ii) tight junctions that separate apical and lateral surface domains and form barriers to the intercellular diffusion of ions and macromolecules; (iii) cohesive cell-cell interactions formed by cell adhesion molecules (CAMs) and a highly developed junctional complex; and (iv) the polarized distribution of cytoplasmic organelles and the cytoplasmic and cortical cytoskeleton.

These structural characteristics are responsible for several biological roles of polarized epithelial cells (*1*) (Fig. 1). (i) Transporting epithelia form selective permeability barriers between the biological compartments (lumen and serosa) of different ionic compositions (*2*). (ii) Transporting and secretory epithelia actively regulate the composition of these biological compartments by carrying out specialized vectorial functions in absorption, transcytosis, and secretion. These vectorial functions depend on the polarized distributions of channels and transport enzymes to the apical and basal-lateral domains of the plasma membrane (*1, 2*). (iii) The cohesive monolayer structure of the epithelium, in which cells are linked together through the junctional complex and the cytoskeletal contractile apparatus, is responsible for the folding of epithelial germ layers during embryo development (for example, during gastrulation and formation of the neural and intestinal tubes) (*3*).

Many of the membrane proteins of polarized epithelial cells are common to nonpolarized cells [for example, the Na^+- and K^+-dependent adenosine triphosphatase (Na^+,K^+-ATPase) and growth factor receptors]. However, their nonrandom distribution on the membrane in polarized epithelial cells is characteristic of the vectorial functions performed by this cell type (*1*). For example, the basal-lateral membrane location of the Na^+,K^+-ATPase and apical membrane location of Na^+ channels results in the generation of a transepithelial gradient of Na^+ that facilitates vectorial uptake and

E. Rodriguez-Boulan is in the Department of Cell Biology and Anatomy, Cornell University Medical College, New York, NY 10021. W. J. Nelson is at the Institute for Cancer Research, Fox Chase Cancer Center, Philadelphia, PA 19111.